Full characterization of RF compressed femtosecond electron pulses using ponderomotive scattering

Meng Gao,[1] **Hubert Jean-Ruel,**[1] **Ryan R. Cooney,**[1] **Jonathan Stampe,**[3] **Mark de Jong,**[3] **Maher Harb,**[1,4] **German Sciaini,**[2] **Gustavo Moriena,**[1] **and R. J. Dwayne Miller**[1,2,*]

[1]*Institute of Optical Sciences and Department of Physics and Chemistry, University of Toronto, 80 St.George St., Toronto, ON, M5S3H6, Canada*
[2]*Max Planck Department for Structural Dynamics, Department of Physics, University of Hamburg, Centre for Free Electron Laser Science, DESY, Notkestrasse 85, Hamburg 22607, Germany*
[3]*Canadian Light Source Inc., 101 Perimeter Road, Saskatoon, SK, S7N 0X4, Canada*
[4]*Present address: Atomic Physics Division, Department of Physics, Lund University, P.O. Box 118, 22100 Lund, Sweden*

[*]*dwayne.miller@mpsd.cfel.de*

Abstract: High bunch charge, femtosecond, electron pulses were generated using a 95 kV electron gun with an S-band RF rebunching cavity. Laser ponderomotive scattering in a counter-propagating beam geometry is shown to provide high sensitivity with the prerequisite spatial and temporal resolution to fully characterize, *in situ*, both the temporal profile of the electron pulses and RF time timing jitter. With the current beam parameters, we determined a temporal Instrument Response Function (IRF) of 430 fs FWHM. The overall performance of our system is illustrated through the high-quality diffraction data obtained for the measurement of the electron-phonon relaxation dynamics for Si (001).

© 2012 Optical Society of America

OCIS codes: (320.2250) Femtosecond phenomena; (320.7100) Ultrafast measurements.

References and links

1. B. J. Siwick, J. R. Dwyer, R. E. Jordan, and R. J. D. Miller, "An Atomic-Level View of Melting Using Femtosecond Electron Diffraction," Science **302,** 1382–1385 (2003).
2. A. M. Lindenberg, J. Larsson, K. Sokolowski-Tinten, K. J. Gaffney, C. Blome, O. Synnergren, J. Sheppard, C. Caleman, A. G. MacPhee, D. Weinstein, D. P. Lowney, T. K. Allison, T. Matthews, R. W. Falcone, A. L. Cavalieri, D. M. Fritz, S. H. Lee, P. H. Bucksbaum, D. A. Reis, J. Rudati, P. H. Fuoss, C. C. Kao, D. P. Siddons, R. Pahl, J. Als-Nielsen, S. Duesterer, R. Ischebeck, H. Schlarb, H. Schulte-Schrepping, Th. Tschentscher, J. Schneider, D. von der Linde, O. Hignette, F. Sette, H. N. Chapman, R. W. Lee, T. N. Hansen, S. Techert, J. S. Wark, M. Bergh, G. Huldt, D. van der Spoel, N. Timneanu, J. Hajdu, R. A. Akre, E. Bong, P. Krejcik, J. Arthur, S. Brennan, K. Luening, and J. B. Hastings, "Atomic-Scale Visualization of Inertial Dynamics," Science **308,** 392–395 (2005).
3. G. Sciaini, M. Harb, S. G. Kruglik, T. Payer, C. T. Hebeisen, F.-J. M. z. Heringdorf, M. Yamaguchi, M. H.-v. Hoegen, R. Ernstorfer, and R. J. D. Miller, "Electronic acceleration of atomic motions and disordering in bismuth," Nature **458,** 56–59 (2009).
4. R. Ernstorfer, M. Harb, C. T. Hebeisen, G. Sciaini, T. Dartigalongue, and R. J. D. Miller, "The Formation of Warm Dense Matter: Experimental Evidence for Electronic Bond Hardening in Gold," Science **323,** 1033–1037 (2009).
5. M. Eichberger, H. Schafer, M. Krumova, M. Beyer, J. Demsar, H. Berger, G. Moriena, G. Sciaini, and R. J. D. Miller, "Snapshots of cooperative atomic motions in the optical suppression of charge density waves," Nature **468,** 799–802 (2010).

6. A. Cavalleri, C. Tth, C. W. Siders, and J. A. Squier, "Femtosecond Structural Dynamics in VO2 during an Ultrafast Solid-Solid Phase Transition," Phys. Rev. Lett. **87,** 237401 (2001).
7. P. Reckenthaeler, M. Centurion, W. Fu, S. A. Trushin, F. Krausz, and E. E. Fill, "Time-Resolved Electron Diffraction from Selectively Aligned Molecules," Phys. Rev. Lett. **102,** 213001 (2009).
8. F. Schotte, M. Lim, T. A. Jackson, A. V. Smirnov, J. Soman, J. S. Olson, G. N. Phillips Jr., M. Wulff, and P. A. Annrud, "Watching a Protein as it Functions with 150-ps Time-Resolved X-ray Crystallography," Science **300,** 1944–1947 (2003).
9. R. C. Dudek and P. M. Weber, "Ultrafast diffraction imaging of the electrocyclic ring-opening reaction of 1,3-cyclohexadiene," J. Phys. Chem. A **105,** 4167-4171 (2001).
10. A. H. Zewail, "4D Ultrafast Electron Diffraction, Crystallography, and Microscopy," Annu. Rev. Phys. Chem. **57,** 65–103 (2006).
11. M. Aidelsburger, F. O. Kirchner, F. Krausz, and P. Baum, "Single-electron pulses for ultrafast diffraction," PNAS **107,** 19714–19719 (2010).
12. G. Sciaini and R. J. D. Miller, "Femtosecond electron diffraction: heralding the era of atomically resolved dynamics," Rep. Prog. Phys. **74,** 096101 (2011).
13. R. J. D. Miller, R. Ernstorfer, M. Harb, M. Gao, C. T. Hebeisen, H. Jean-Ruel, C. Lu, G. Moriena, and G. Sciaini, "'Making the molecular movie': first frames," Acta. Crystallogr. Sect. A **A66,** 135–156 (2010).
14. B. J. Siwick, J. R. Dwyer, R. E. Jordan, and R. J. D. Miller, "Ultrafast electron optics: Propagation dynamics of femtosecond electron packets," J. Appl. Phys. **92,** 1643–1648 (2002).
15. W. E. King, G. H. Campbell, A. Frank, B. Reed, J. F. Schmerge, B. J. Siwick, B. C. Stuart, and P. M. Weber, "Ultrafast electron microscopy in materials science, biology, and chemistry," J. Appl. Phys. **97,** 111101 (2005).
16. G. H. Kassier, K. Haupt, N. Erasmus, E. G. Rohwer, and H. Schwoerer, "Achromatic reflectron compressor design for bright pulses in femtosecond electron diffraction," J. Appl. Phys. **105,** 113111 (2009).
17. T. v. Oudheusden, E. F. d. Jong, S. B. v. d. Geer, W. P. E. M. O. t. Root, O. J. Luiten, and B. J. Siwick, "Electron source concept for single-shot sub-100 fs electron diffraction in the 100 keV range," J. Appl. Phys. **102,** 093501 (2007).
18. T. v. Oudheusden, P. L. E. M. Pasmans, S. B. v. d. Geer, M. J. d. Loos, M. J. v. d. Wiel, and O. J. Luiten, "Compression of Subrelativistic Space-Charge-Dominated Electron Bunches for Single-Shot Femtosecond Electron Diffraction," Phys. Rev. Lett. **105,** 264801 (2010).
19. C. T. Hebeisen, G. Sciaini, M. Harb, R. Ernstorfer, T. Dartigalongue, S. G. Kruglik, and R. J. D. Miller, "Grating enhanced ponderomotive scattering for visualization and full characterization of femtosecond electron pulses," Opt. Express **16,** 3334–3341 (2008).
20. "General Particle Tracer," `http://www.pulsar.nl/gpt`.
21. C. T. Hebeisen, R. Ernstorfer, M. Harb, T. Dartigalongue, R. E. Jordan, and R. J. D. Miller, "Femtosecond electron pulse characterization using laser ponderomotive scattering," Opt. Lett. **31,** 3517–3519 (2006).
22. S. Tokita, M. Hashida, S. Inoue, T. Nishoji, K. Otani, and S. Sakabe, "Single-Shot Femtosecond Electron Diffraction with Laser-Accelerated Electrons: Experimental Demonstration of Electron Pulse Compression," Phys. Rev. Lett. **105,** 215004 (2010).
23. P. L. Kapitza and P. A. M. Dirac, "The reflection of electrons from standing light waves," Math. Proc. Camb. Philos. Soc. **29,** 297–300 (1933).
24. D. L. Freimund, K. Affatooni, and H. Batelaan, "Observation of the Kapitza-Dirac Effect," Nature **413,** 142–143 (2001).
25. M. Harb, R. Ernstorfer, T. Dartigalongue, C. T. Hebeisen, R. E. Jordan, and R. J. D. Miller, "Carrier Relaxation and Lattice Heating Dynamics in Silicon Revealed by Femtosecond Electron Diffraction," J. Phys. Chem. B **110,** 25308–25313 (2006).
26. M. Harb, W. Peng, G. Sciaini, C. T. Hebeisen, R. Ernstorfer, M. A. Eriksson, M. G. Lagally, S. G. Kruglik, and R. J. D. Miller, "Excitation of longitudinal and transverse coherent acoustic phonons in nanometer free-standing films of (001) Si," Phys. Rev. B **79,** 094301 (2009)
27. Y. Murooka, N. Naruse, S. Sakakihara, M. Ishimaru, J. Yang, and K. Tanimura, "Transmission-electron diffraction by MeV electron pulses," Appl. Phys. Lett. **98,** 251903 (2011).

---

1. Introduction

The dream of atomically resolved structural dynamics has become a reality with the recent advent of high brightness electron [1] and x-ray sources [2]. Ultrafast electron and x-ray diffraction have both demonstrated success in resolving many fundamental questions in physics [3–6], chemistry [7], and biology [8]. There is great interest in pushing the time resolution to the 10 femtosecond domain with sufficiently high flux to capture even the fastest nuclear motions involved in chemical and biological reactions. For electrons, the primary challenge was to overcome the effects of space-charge broadening, imposing a fundamental trade-off between

electron density and pulse duration. For non-relativistic electrons, the main approach to bring electron diffraction to the fs regime was to either significantly sacrifice bunch density for high (kHz - MHz) repetition rates [9–11], or use a compact electron gun concept to conserve moderate bunch charge densities [1]. The minimum number of electrons to achieve atomic resolution is typically on the order of 10^4 electrons for high-Z systems and small unit cells. These requirements increase with the size of the unit cell and smaller Z materials. For irreversible samples and semi-reversible samples, the finite number of photo-excitation cycles severely limits the use of high repetition rate, low density sources. However, even for reversible samples, there are problems with rapid photo-excitation. For example, in many materials with poor thermal conductance (most organic samples), the time scales for the dissipation of heat from the laser excitation can range from hundreds of microseconds to hundreds of milliseconds, rendering MHz and even kHz probe sources unusable. In this regard, the importance of high intensity structural probes has been amply demonstrated with the large number of systems that can be studied at atomic resolution within the single shot limit using the compact electron gun concept [12, 13]. The importance of high intensity sources for structural probes is also well appreciated in the x-ray community and has been a driving force in the development of next generation light sources.

In terms of scaling non-relativistic electron sources to higher intensities, the key new insight that came from an effectively exact solution to the electron propagation dynamics at high charge density was the realization that non-relativistic electrons naturally develop an extremely linear chirp in relatively short propagation distances [14]. The initial spatial correlations in the longitudinal direction are conserved up to very high bunch charge densities and the energy dependence of the velocity distribution in the non-relativistic regime creates a highly linear velocity-spatial correlation in the electron bunch. Given the high linearity in the chirp, this work pointed out that it should be fairly straightforward to use standard compression methods to reverse the linear chirp and dramatically increase the electron source brightness [14]. There are various methods from reflectron designs to dispersive chicane bunchers that are formally equivalent to prism pairs in optics for dispersion compensation [15, 16]. A particularly elegant solution was proposed that takes advantage of high electric field gradients possible within a half cell RF cavity or standard pill lens to invert the velocity spread in the electron distribution [17]. This approach provides compression solely along the propagation axis and removes spatial chirp issues. Numerical modelling of the RF compression illustrated the pill lens method has the potential to produce low-emittance, sub-100 fs, 0.1-1 pC bunches at the sample position, a dramatic improvement in brightness and pulse duration. The drawback with this approach is that the system becomes highly susceptible to RF phase noise, which ultimately limits the timing resolution of the instrument. In all cases, pulse compression of non-relativistic electron pulses leads to a strong dependence of the pulse duration along the beam propagation path. New means of characterizing the temporal profile of this class of electron pulses is needed to enable precise determination of the instrument response, ideally with 10 femtosecond time resolution and sub-100 micron spatial resolution to meet all design criteria.

The RF pulse compression method using a pill lens has recently been demonstrated [18] using a synchronized RF streak camera for characterizing the pulse-compression process. However, the RF-laser timing jitter is difficult to decouple in these measurements as the arrival time is much more sensitive to changes in the RF phase (near $\phi = 0$) than the pulse width. It is fully expected that the biggest challenge in exploiting RF pulse compression methods to obtain the highest possible time resolution is the inherent difficulty in minimizing this timing jitter. Thus, for femtosecond electron diffraction experiments using RF compression systems, it is no longer sufficient to only determine the electron pulse duration, but rather the temporal Instrument Response Function (IRF), which includes the full convolution of the electron and laser pulses, as

well as factors affecting RF timing jitter. In this paper, we use the counter-propagating grating enhanced ponderomotive scattering method [19] with the aforementioned temporal and spatial resolution to directly probe the IRF of our RF pulse compression system. The higher bunch charge density in this new regime allows high quality femtosecond diffraction data to be collected with orders of magnitude fewer excitation cycles, opening the door to the study of irreversible processes and ultrafast chemical reactions in organic and biological systems. The high diffraction quality and temporal resolution of the system is clearly demonstrated by measuring the photo-carrier relaxation dynamics into lattice phonons for single crystalline silicon, as will be shown below.
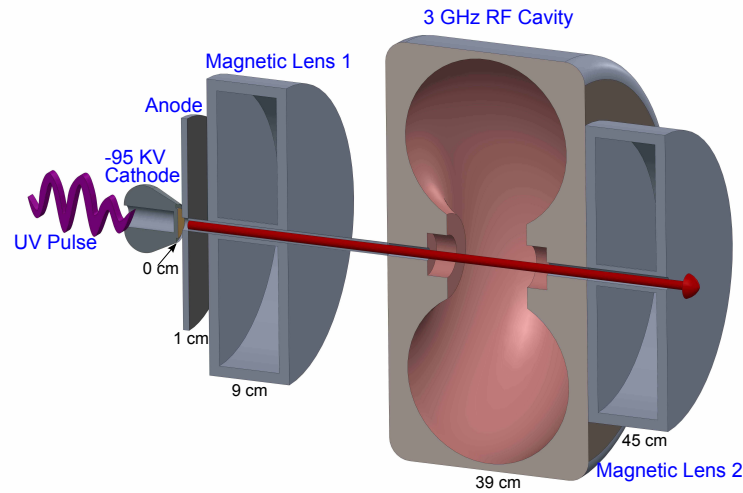
2. RF pulse compression system

Fig. 1. General Schematic of the Two Lens Hybrid DC-RF Pulse Compression System. A 270 nm UV pulse back-illuminates a gold photo-cathode and generates an electron pulse with a bunch charge up to 200 fC. The electron bunch is accelerated through a 95 keV extraction field, collimated by the first magnetic lens, rebunched in the 3 GHz RF cavity, and then collimated again towards the sample by a second magnetic lens. The electron-optic elements are labelled and their respective distances are given in cm from the cathode.

A schematic of the electron gun is shown in Fig. 1. UV back-illumination of a gold photo-cathode generates a dense electron pulse ($100e^-$ per μm^2) that is subsequently accelerated at 95 keV toward a Si disk anode with a 700 μm aperture. The silicon is boron-doped for high electrical conductivity to avoid charge accumulation, and polished to optical flatness to avoid high-voltage discharges. Space-charge broadening during propagation quickly imposes a linear chirp [14] on the electron pulse within a few centimetres of travel. The exceptionally highly linear nature of this chirp makes it possible to compress the pulse by a sinusoidally time varying electric field synchronized with the arrival of the electron pulse. The time-dependent electric field for this purpose is generated by the standing wave TM_{010} mode at $f = 2.998$ GHz of our cylindrically symmetric RF cavity. The cavity geometry was optimized to efficiently couple in RF power such that a solid state amplifier can be used instead of a klystron typically used for higher power requirements. The duty cycle load limit of the amplifier restricts operation to un-

der 100 Hz. However, our setup is currently optimized for 10 Hz to avoid sample heating issues. We can switch to 100 Hz without major modifications. To synchronize the oscillator with the RF signal, we use an electronic synchronization system (Acctec B.V.), which picks off a high harmonic from the laser oscillator pulse train using a fast photodiode and phase locks a 3 GHz VCO (Voltage Controlled Oscillator) output that drives the RF cavity after amplification. The longitudinal electric field inside the cavity is given by:

$$E_z = E_0 sin(2\pi ft + \phi_0).$$ (1)

The phase, ϕ_0, must be carefully tuned such that the center of the electron pulse is passing the center of the cavity when $E_z = 0$. This phase relationship ensures that the front edge of the pulse experiences a decrease in velocity; while the back edge experiences an increase, and there is no net energy gained by the entire pulse. The curvature in the field lines at the entrance and exit points of the cavity produce a net defocusing effect in the transverse direction. Thus, a second magnetic lens is required to re-focus the electron beam towards the sample position. GPT [20] (General Particle Tracer) simulations have demonstrated that this system is able to achieve sub-100 fs pulse durations with approximately 5 nm transverse coherence at the sample position.

3. Ponderomotive measurement system

The experimental setup for the counter-propagating grating based ponderomotive scattering method is shown schematically in Fig. 2. The temporal response of this approach is only limited by the laser focusing geometry and the laser pulse duration, implying 10 fs temporal resolution is achievable with conventional femtosecond laser systems with reasonable focusing conditions [21]. The electron pulse is effectively cross correlated with the known laser pulse through the spatial perturbation imposed on the electron distribution by the laser induced ponderomotive potential. In this respect, the ponderomotive force describes the process by which a charged particle in an inhomogeneous oscillating electric field drifts towards the weak field region. It is proportional to the gradient of the light intensity [19], i.e.

$$\mathbf{F}(\mathbf{r},t) = -\frac{e^2\lambda^2}{8\pi^2 m_e \varepsilon_0 c^3}\nabla I(\mathbf{r},t);$$ (2)

where λ is the laser wavelength, ε_0 is the permittivity of vacuum, and $I(\mathbf{r},t)$ is the spatial-temporal dependence of the light intensity. For reasonable 800 nm Ti:Sapphire laser parameters (100 fs, 10 μm focus), tens of millijoules of pulse energy are required to produce a detectable ponderomotive signal using a single beam interaction [21,22]. This power requirement exceeds the capabilities of small frame laser systems. Previously, we demonstrated that the effective interaction can be dramatically increased by adopting a counter-propagating beam geometry to form a standing wave with the maximum number of fringes in the interaction region. The strong spatial modulation in the light intensity along the grating direction increases the intensity gradient by several orders of magnitude. The effect was first predicted by Kapitza and Dirac in 1933 [23,24]. This optical grating produces a comb of scattering centers with a periodicity of half the wavelength of the light.

Given the many complex tuning parameters (amplitude, phase, temperature etc.) of the RF electron pulse compression system, we designed a compact modular setup that can be used on a day-to-day basis, requires minimal effort for alignment, and can be used *in situ* with pump probe measurements. The entire device, as schematically shown in Fig. 2 is built on a 5″ by 7″ breadboard, weighs <2 kg, and rests entirely in vacuum (at 10^{-8} torr) on 3-axis translation stages. The path length between the beamsplitter and the scattering point is only
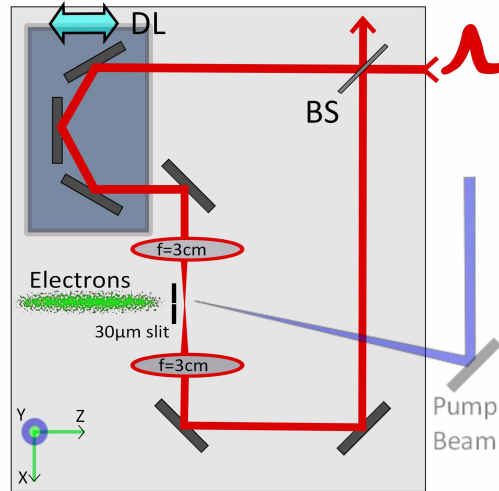
Fig. 2. Compact Grating Enhanced Ponderomotive Cross Correlation Setup. This compact system allows *in situ* measurements of the electron pulse duration and timing jitter in the t=0 position, essential to fully determining the true time resolution in the use of electron probes to atomically resolve structural dynamics (DL = motorized delay line; BS = beam splitter).

20 cm, making the transient grating highly insensitive to pointing instabilities. Samples can be mounted directly underneath and in the same plane as the ponderomotive scattering region to allow quick switching between pump probe experiments and ponderomotive measurements. A laser pulse (300 μJ, 50 fs, 800 nm) is split into two paths by a 50/50 beamsplitter (BS). The first path (upper) passes by a delay line (DL) for path length matching. Both beams are focused by 3 cm lenses to $10\pm3\mu$m FWHM (Full Width Half Maximum) spots at the interaction region. The spot sizes are measured with a knife edge directly at the interaction region. The electron beam propagates 11 cm from the center of the RF cavity to the sample position where it is stripped by a 30 μm slit before scattering from the ponderomotive grating. The slit is placed 8 mm before the scattering region to avoid contact with the laser grating. Since the transverse length (x-axis) of the grating is only 15 μm (50 fs), the slit removes the majority of unscattered electrons that do not contribute to the ponderomotive signal. This procedure removes the background to greatly facilitate detection of the ponderomotive effect on the electron distribution. The final signal is picked up by a phosphor-plated CCD detector.

4. Ponderomotive scattering results

4.1. *Ponderomotive signal and instrument response measurement*

Figure 3 shows the ponderomotive scattering signal for a given time delay such that the maxima of the laser grating is formed in the center of the electron bunch (middle), and no signal is seen when the grating is formed before (left) or after (right) the arrival of the electron bunch. To extract the IRF information from the images, we used the method from *Hebeisen et al.* [19].

$$S(t) = \int |X| D_t(X,Y) dX dY. \tag{3}$$

Equation (3) defines the scattering signal S at time delay t which is given by the integration of the pixel intensities weighted by the scattered distance X from the center. Figure 4(a) shows $S(t)$ for the optimally compressed pulse for a 200 fC bunch. We determined the optimum amplitude
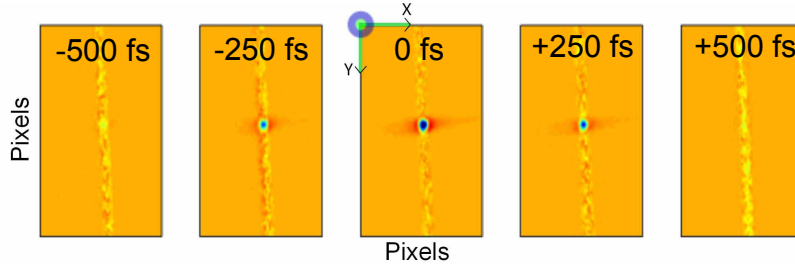
Fig. 3. The ponderomotive signal for a 200 fC bunch charge stripped by a 30 μm slit at various time delays, as indicated (-500 fs to +500 fs). The field amplitude inside the cavity is 0.67 MV/m. At optimal temporal overlap between the ponderomotive grating and the electron beam (0 fs), the electron are almost entirely depleted from the center and scattered in the transverse direction. The color code is chosen to provide a difference map of the electron spatial distribution with and without laser excitation; where the intensity in the blue color represents a negative change in density and the red color represents positive change in density. The slit appears slightly tilted due to the detector orientation. These images are scaled to fit the margins of the paper and do not represent the scale of the original data.

by varying the field amplitude inside the cavity and found the minimum IRF. Figure 4(b) shows the measured compression curve for different RF field amplitudes. The most meaningful figure of merit that can be extracted from the time-dependent scattering signal is the effective electron pulse duration $\sigma_{\mathbf{eff}}$, which is a convolution between the true electron pulse duration and the timing jitter. Since the transit time of the electron pulse across the transient grating broadens the ponderomotive signal, we must first remove these contributions to recover $\sigma_{\mathbf{eff}}$. We can assume that the laser is Gaussian shaped in both longitudinal and transverse directions such that the deconvolution of the geometrical factors is simple:

$$\sigma_{\mathbf{eff}}^2 = \sigma_S^2 - \sigma_{\mathbf{t-laser}}^2 - \sigma_{\mathbf{w-laser}}^2/v_{\mathbf{electron}}^2; \tag{4}$$

where $\sigma_{\mathbf{t-laser}}$ and $\sigma_{\mathbf{w-laser}}$ are the laser pulse duration, and spot size, respectively, and $v_{\mathbf{electron}}$ is the electron velocity. The deconvolution also sets a lower limit on the resolution of our measurement due to the transit time of the electrons across the laser pulse. For 50 fs FWHM laser pulses, focused to a 10 μm FWHM spot size, the resolution is approximately 35 fs (in σ). For the optimal RF field amplitude, we measure an effective pulse duration of 430 ± 75 fs FWHM. Since our laser pulse duration is 50 fs FWHM (much smaller than $\sigma_{\mathbf{eff}}$), this value represents a direct measure of the temporal instrument response in a pump-probe experiment. We note here that this measurement is broader than that inferred using streak camera measurements [18]. We attribute this difference to the fact that the streak camera measurements do not provide a direct measure of the IRF but rather information on the electron pulse duration.

4.2. Long term stability and jitter measurement

The IRF is determined by both the electron and laser pulse durations, as well as the timing jitter between the electron and laser pulses. There are two major contributions to the timing jitter: a) temperature drifts slowly changing path lengths and phases of the RF components leading to slow variations in the average time trace; and b) electronic noise, mechanical vibrations, and laser cavity instabilities that lead to fast variations in the phase of the RF. The former case, (a), can be fixed by temperature stabilizing the RF electronics, the RF cavity, and cables etc. Figure 5 shows considerably improved performance of the system over 1.5 hours of operation after
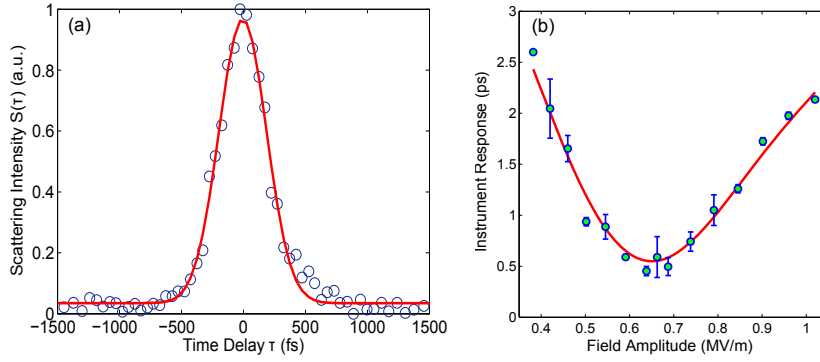
Fig. 4. (a) The time averaged scattering signal $S(\tau)$ is obtained with 200 shots per point for a 200 fC bunch charge. This results in an IRF of 430 ± 75 fs FWHM following deconvolution using Eq. (4). The field amplitude is 0.67 MV/m. (b) The IRF measured by ponderomotive scattering vs field amplitude at $E_z(0, r = 0)$. The minimum in the field dependence corresponds to the cross correlation shown in (a). The red line is a smoothing curve to illustrate the shape of the focus.

temperature stabilization. The latter case, (b), is more difficult to control as it also limits the intrinsic IRF of the system. Since we operate our RF cavity at 10 Hz, any phase jitter will be effectively integrated in the noise spectrum > 10Hz and show up as shot-to-shot noise in the ponderomotive signal.

We can examine the distribution of ponderomotive signal intensities to estimate the high frequency or fast jitter characteristics. Empirically, the distribution of the scattering signal for a given time t should be a function of the timing jitter width σ_j and the pulse duration σ_t assuming the jitter has a gaussian distribution with a mean at the center of the pulse and variance σ_j^2. We can model the ponderomotive scattering signal with the inclusion of jitter by:

$$Y(t) = Ae^{-\frac{(t-J)^2}{2\sigma_t^2}} ; \qquad (5)$$

where J is a random variable with distribution function $f_J(j) = \text{Norm}(0, \sigma_j^2)$. Then we can perform a transformation by the CDF (Cumulative Distribution Function) method to find the distribution function for $Y(t)$ using $f_Y(y) = \frac{d}{dy}F_j(Y^{-1}(y))$. The result depends only on the ratio σ_j/σ_t and the position of t. A subset of the solution is shown in Fig. 6(a) for $t = 0$. Taking $\alpha = \sigma_j/\sigma_t$, then for the case $\alpha \ll 1$ (the case where jitter is small compared to the pulse width), the signal is very stable and distributed close to the maximum signal (unity). For the case $\alpha \gg 1$, the jitter is large and the signal is rarely seen so it is more closely distributed around 0. Since both the pulse duration and the jitter are gaussian shaped in their respective temporal distributions, we know the effective pulse duration $\sigma_{\text{eff}}^2 = \sigma_t^2 + \sigma_j^2$, we can fit the distribution as a function of α and t, and therefore extract a value for σ_j.

To extract the fast jitter, we made a series of fast single shot scattering measurements in succession (several minutes) to avoid slow timing drifts as much as possible and examined the resultant distribution of intensities. To minimize contributions from the background, the measured signal is the differential amplitude between a portion of the slit where the scattering occurs and where it is absent. Figure 6(b) shows the normalized histogram of the measured signals. We performed a least squares fit in a 2 parameter space of (α, t) with the constraint $\sigma_{\text{eff}}^2 = \sigma_t^2 + \sigma_j^2$ and converged on the result shown by the red line in Fig. 6, giving $\alpha = 0.28 \pm 0.05$ and $t = 238 \pm 30$ fs. This fit results in a fast jitter value of 125 ± 70 fs FWHM. This
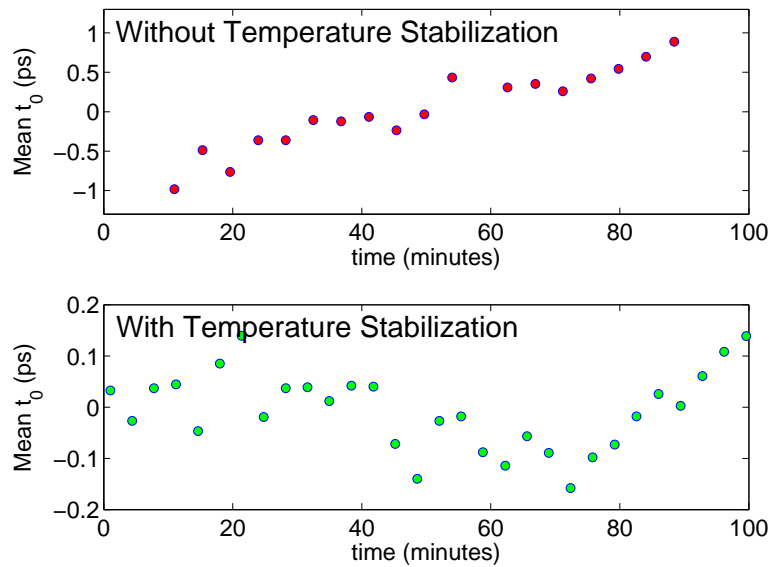
Fig. 5. Effect of Temperature Stability on Timing Jitter. Successive ponderomotive traces were taken on 3 minute intervals. The top plot shows temperature instabilities leading to a large overall phase drift of 2 ps over the course 1.5 hours. The bottom plot shows that after temperature stabilizing the RF electronics and cables, we were able to maintain average t_0 stability of 70 fs RMS (Root Mean Squared) over the course of the same period of time.

determination represents a lower limit as there are drift contributions during the measurement that must be properly statistically weighted. The most important parameter with the respect to time resolution is still the IRF that takes all contributions to the effective time resolution into account.

5. Electron-phonon dynamics in silicon

To demonstrate both the temporal resolution and the ability to perform pump-probe experiments, we measured the ultrafast heating (Debye-Waller) dynamics of single crystalline silicon. In this case, we used 40 fC per pulse and focused the electron beam to $200 \pm 20 \mu$m FWHM at the sample position. The signal was collected with 10 shots (total 400 fC) to produce the high-quality diffraction pattern in Fig. 7(a). We pumped the sample with 400 nm laser pulse at a fluence of 3.5 mJ/cm^2, well below the damage threshold, and recovered the structure dynamics shown in Fig. 7(b). The bi-exponential fit of $\tau_1 = 880 \pm 110$ fs and $\tau_2 = 9 \pm 0.9$ ps shows good agreement with previous measurements at comparable excitation intensities [25, 26]. In the previous experiment by Harb et. al [25], the diffraction quality was only sufficient to fit to a single relaxation component that would weigh the decay to longer values as observed in comparing the two results. Here we are able to clearly observe two relaxation time scales in the lattice dynamics. This experiment shows that extremely high quality diffraction patterns can be collected with merely a few shots. Equally important, the excellent SNR, even with this low number of shots per time point, enabled the observation of a multicomponent relaxation process involving the initial relaxation of photocarriers into optical phonon lattice modes (fast component) followed by subsequent optical phonon acoustic mode coupling (slow component) that
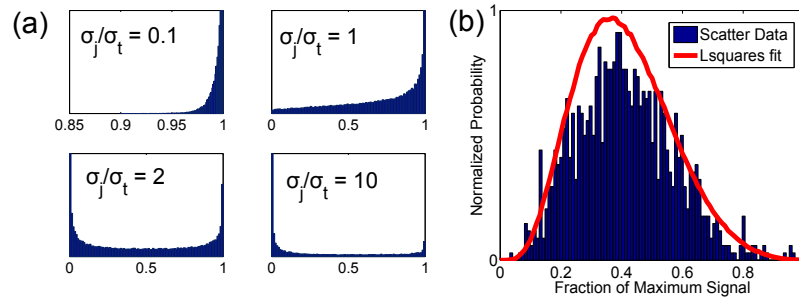
Fig. 6. Timing Jitter Measurement. (a) simulated distributions $f_Y(y)$ for the scattering signal at $t = 0$ for a given ratio of the jitter to the pulse width $\alpha = \sigma_j/\sigma_t$ and setting $\sigma_{eff}^2 = \sigma_t^2 + \sigma_j^2$. (b) The measured distribution for a given time t normalized such that the maximum signal is 1. The least squares fit (red line) gives $\alpha = 0.28 \pm 0.05$ and $t = 238 \pm 30$ fs

give different RMS atomic displacements. This work should be compared to the similarly high quality, static, diffraction results obtained recently with a relativistic source [27] for Si. In this respect, the quality of the time-resolved diffraction orders in the present case is notable. Here, we are able to obtain comparable quality of diffraction patterns out to even higher diffraction orders and have been able to resolve the relatively small amplitude displacements involved in the slower relaxation processes of optical phonons into acoustic modes.
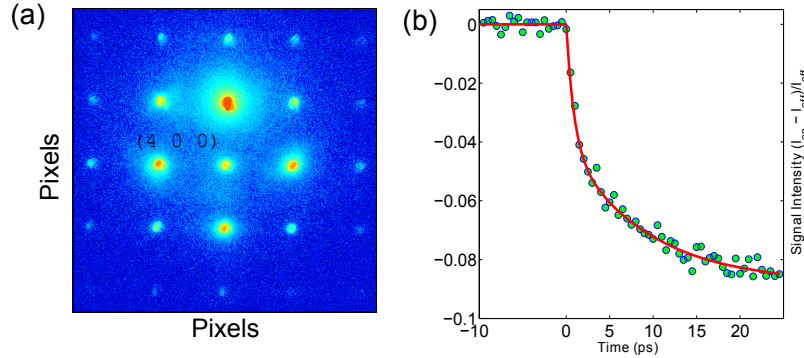

Fig. 7. Femtosecond Electron Diffraction Study of Photocarrier-Lattice Relaxation Dynamics in Si(001).(a) Diffraction pattern of single crystal silicon collected from 10 shots (40 fC per shot), $200 \pm 20\ \mu m$ FWHM electron beam. (b)Photocarrier relaxation into lattice phonons is clearly observed as a decrease in the intensity of the (400) peak with increased RMS motion of the atoms.

6.   Conclusion

We demonstrated the temporal compression of 200 fC electron bunches by using an RF rebunching cavity. The grating enhanced ponderomotive method was used to fully characterized the IRF and jitter properties of this system. With the present state of the system, the system gives an IRF of 430 ± 75 fs FWHM, and is stable over time periods sufficiently long to collect high quality diffraction patterns with less than 200 fs time resolution (i.e. one standard deviation of the FWHM IRF) as exemplified by the data obtained for single crystal Si(001). This

work illustrates the importance in fully characterizing the system response function. With improvements to the electronic synchronization, using additional phase lock loops to control laser frequency stability, and better RF amplitude and phase optimization, it should be possible to achieve sub-100 fs FWHM temporal resolution with a high intensity compact electron source. This system has now achieved high enough bunch charge densities and time resolution to open up atomically resolved reaction dynamics of even complex, low Z, materials such as organic molecules and proteins that are generally irreversible.

Acknowledgments